THE JOURNAL OF PHYSICAL CHEMISTRY Letters

Spectroscopy and Photochemistry; General Theory

Hydrogen Bonding Induced Morphology Dependence of Long-lived Organic Room-Temperature Phosphorescence: A Computational Study

Huili Ma, Hongde Yu, Qian Peng, Zhongfu An, Dong Wang, and Zhigang Shuai

J. Phys. Chem. Lett., **Just Accepted Manuscript** • DOI: 10.1021/acs.jpclett.9b02568 • Publication Date (Web): 25 Oct 2019

Hydrogen Bonding Induced Morphology Dependence of Long-lived Organic Room-Temperature Phosphorescence: A Computational Study

Huili Ma,[†] *Hongde Yu,*[§] *Qian Peng,**[,‡] *Zhongfu An,*[†] *Dong Wang,*[§] *and Zhigang Shuai**[§]

[†]Key Laboratory of Flexible Electronics (KLOFE) and Institute of Advanced Materials (IAM), Nanjing Tech University, Nanjing 211816, P. R. China

[§]Key Laboratory of Organic OptoElectronics and Molecular Engineering, Department of Chemistry, Tsinghua University, Beijing 100084, P. R. China

[‡]Key Laboratory of Organic Solids, Beijing National Laboratory for Molecular Science (BNLMS), Institute of Chemistry, Chinese Academy of Sciences, Beijing 100190, P. R. China

AUTHOR INFORMATION

Corresponding Authors

*Qian Peng. Tel: +86-10-82616830. E-mail: qpeng@iccas.ac.cn.

*Zhigang Shuai. Tel: +86-10-62797689. E-mail: zgshuai@tsinghua.edu.cn.

ABSTRACT: Organic room-temperature phosphorescence (RTP) generally only exhibits in aggregate with strong dependence on morphology, which are highly sensitive to the intermolecular hydrogen bonding interaction. Here, 4,4'-bis(9H-carbazol-9-yl)methanone (Cz2BP), emitting RTP in cocrystal consisting of chloroform but not in amorphous nor in crystal, was investigated to disclose the morphology dependence through molecular dynamics simulations and first-principles calculations. We find that the strong intermolecular C=O···H-C hydrogen bonds between Cz2BP and chloroform in cocrystal decrease the non-radiative decay rate of $T_1 \rightarrow S_0$ by 3-6 orders of magnitude due to the vibronic decoupling effect on the C=O stretching motion and the increase of (π,π*) composition in T_1 state. The former is responsible for high efficiency and the latter for long-lived RTP with a calculated lifetime of 208 ms (exp. 353 ms). Nevertheless, the weak hydrogen bonds cannot cause any appreciable RTP in amorphous and crystal. This novel understanding opens a way to design organic RTP materials.

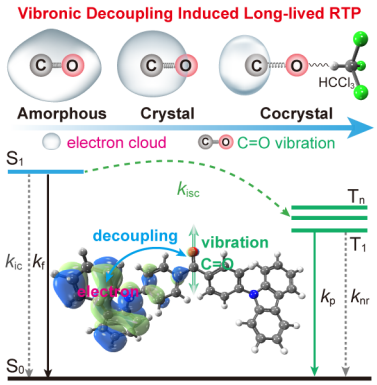

Organic materials with persistent room-temperature phosphorescence (RTP) have aroused strong interests owing to the potential applications in bioimaging, data encryption, light-emitting, information display, and optical recording devices.[1-8] RTP from pure organic molecules always depends on aggregation morphology.[9-15] Even polymorphs with different molecular packing arrangement can demonstrate different RTP behaviors.[10,13] To date, many efforts have been devoted to elucidate the origin of aggregation morphology-dependent RTP behaviors. Several groups believed that the rigid environments in aggregates are favorable for the bright organic solid-states RTP, e.g., crystal, host-guest systems and self-assembled aggregates, owing to the restriction of molecular motions.[16-25] Huang and coworkers suggested that H-aggregated molecules can stabilize the triplet excitons, boosting the long-lived RTP up crystallization,[26] and a similar point of view was proposed by Lucenti *et al.* based on the investigation for the cyclic triimidazole derivatives.[27] Nevertheless, Li *et al.* claimed that the π-π stacking rather than H-aggregation are mainly responsible for the RTP in 10-phenyl-10H-phenothiazine-5,5-dioxide-based derivatives.[28] Chi and coworkers speculated that the intermolecular electronic coupling between the carbonyl and carbazole units enhance the ISC rate, leading to a long-lived RTP.[29] We proposed that intermolecular electrostatic interaction can largely change the composition of the low-lying excited singlet and triplet states, leading to a controllable RTP in organic molecules that contains *n*-electron and π-electron units.[30] These diverse views on organic RTP indicate that it still remains a formidable challenge to revealing the intrinsic mechanism of morphology-dependent RTP.

Very recently, the importance of intermolecular hydrogen bonding interaction on RTP behaviors has come to the attention of researchers. Yuan and coworkers found that the RTP

efficiency and lifetime can be promoted from aromatic esters to acids, this may be ascribed to the strong intermolecular hydrogen bonding in crystal of aromatic acids.[19, 31] Interestingly, the RTP can also be observed in proteins,[32] cocrystal,[9, 33] self-assembled aggregates,[12] owing to the strong intermolecular hydrogen bond in the solid phases. Moreover, aggregation morphology is highly sensitive to the intermolecular hydrogen bonding interactions, it can vary from amorphous to crystal, even to cocrystal by involving solvent molecules.[34] Therefore, it is urgent to quantitatively expound the impact of the intermolecular hydrogen bonding interaction on morphology-dependent organic RTP.

The 4,4'-bis(9H-carbazol-9-yql)methanone (Cz2BP, see Figure 1) possesses persistent RTP (τ_p=353 ms) in cocrystal (Cz2BP:TCM=1:1) with chloroform (TCM) but disappeared in amorphous and crystal phases.[9] In Cz2BP:TCM cocrystal, there are strong intermolecular hydrogen bonds between the Cz2BP and TCM. Therefore, the Cz2BP in the amorphous, crystal and cocrystal phases is a good protype to quantitatively expound the dependence of RTP on the hydrogen bonding interaction. We thus take Cz2BP as an example to quantitatively calculate all the involved excited-state decay rates involving in the RTP process by combining molecular dynamics (MD) simulations, crystal structure prediction, time-dependent density-functional theory (TDDFT) coupled with the thermal vibration correlation function (TVCF) formalism, and explore the origin of the morphology-dependent RTP, especially the relationship between RTP and the intermolecular hydrogen bond strength.

Aggregation morphology of Cz2BP

We firstly produced the amorphous Cz2BP aggregate structure by using MD simulations and then predicted the crystalline Cz2BP structure by combining Polymorph Predictor in close comparison with the experimental X-ray powder diffraction (XRPD)[35,36]; see Figures 1 and S1-S3. The MD simulations were performed with general amber force field (GAFF) for 20 ns with a time step of 2 fs and a configuration storage period of 2 ps for statistical analysis for a cubic box of 15 nm × 15 nm × 15 nm. From Figure S4, it is seen that the volumes of Cz2BP aggregates of five trajectories quickly decrease within 1 ns, and then reach an equilibrium within 10 ns, and the structures are extracted within the final 2 ns for the analysis of the packing density and the radial distribution functions (RDFs). For crystalline Cz2BP, we prepared thousands of trial crystal structures and plotted the density of these trial structures in *P*-1 space group, and selected six crystal structures with lower energy and higher packing density for comparison between simulated XPRD and experimental counterpart in Figures S1-S3. Eventually, one crystal structure wins out for its best match between theoretical and experimental data. Then, this crystal structure was further optimized by periodic density functional theory using PBE-D3(bj) functional and refined through Rietveld refinement algorithm, and its XRPD well reproduced the experimental one, as displayed in Figure 1b. Subsequently, the simulated amorphous and crystal structure with cell parameters (a = 3.975 Å, b = 17.725 Å, c =18.828 Å, α = 88.34°, β = 101.92°, γ = 82.83°) were displayed in Figure S4. In addition, the cocrystal conformation was also optimized using PBE-D3(bj) functional starting from experimental one.

We then look at the morphology (Figures 1, S4 and S5): packing density, averaged radial distribution functions (RDF *vs*. the intermolecular C=O···H-C distance), the packing modes and the intermolecular interaction. From amorphous, crystal to cocrystal, the packing density increases from 1.158, 1.324 to 1.505 g/cm^3, indicating that the molecular packing in cocrystal is the densest.

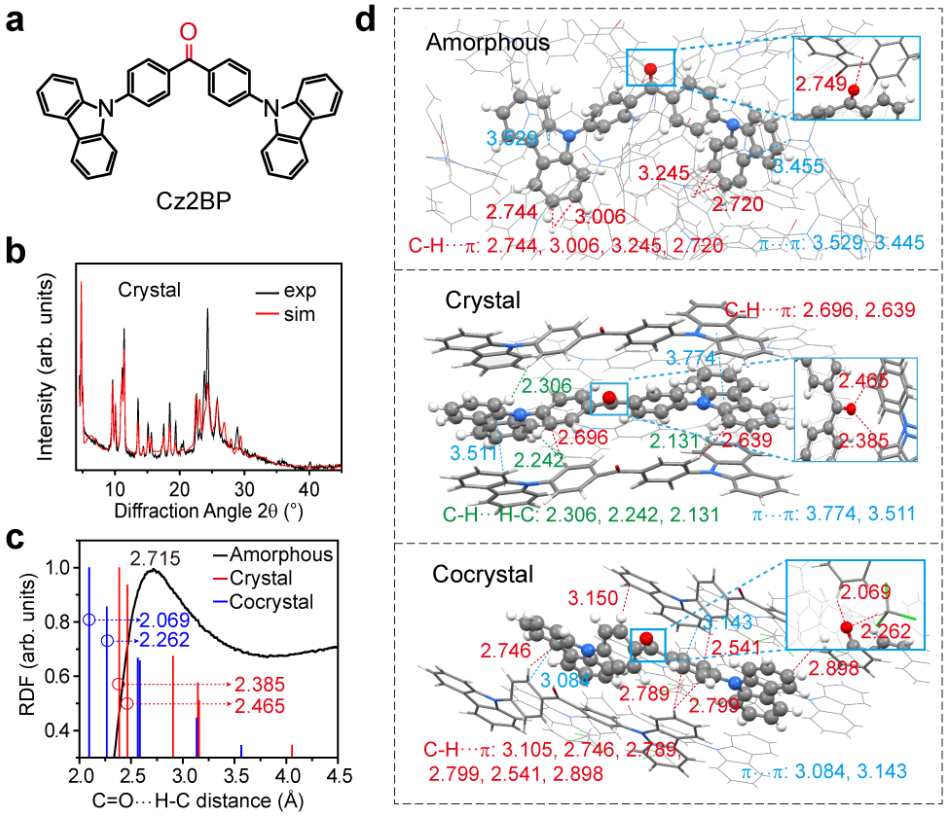

Figure 1. (a) Chemical structure of Cz2BP. (b) XRPD pattern of Cz2BP after refinement together with the experimental values and a difference plot. (c) The average radial distribution functions (RDFs) as a function of the intermolecular C=O···H-C distance for amorphous, crystal and cocrystal. (d) Perspective view of molecular packing in amorphous, crystal and cocrystal for Cz2BP. The unit is angstrom (Å).

We note that from our previous work that excited state composition is sensitive to the intermolecular C=O···H-C distance.[30] We then makes average on RDFs for Cz2BP in three

aggregates as depicted in Figure 1c. It is noted that the amorphous conformations are extracted within the final 2 ns. It is found that the RDFs of Cz2BP amorphous with one major peak around 2.715 Å are larger than that of crystal (2.385 and 2.465 Å) and cocrystal (2.069 and 2.262 Å). Five representative snapshots (A0-A4) were randomly extracted from the amorphous trajectories, in which the smallest intermolecular H-bond distances are all around at the RDFs peak 2.715 Å (see Figure 1d and S5), indicating the chosen amorphous conformations are representative. Focusing on these specific aggregates from amorphous, crystal to cocrystal (Figure 1d and S5), it is seen that in amorphous phase, the molecular packing are disordered and the shortest C=O···H-C distance (2.977 Å for A0, 2.908 Å for A1, 3.043 Å for A2, 2.749 Å for A3, and 2.488 Å for A4, see Figure 1d and S5) is the largest, indicating a weak intermolecular interaction. For the crystalline phase, the molecular packing becomes tight and many forms of intermolecular interaction appear (Figure 1d), such as C=O···H-C (2.465, 2.385 Å), C-H···π (2.696 and 2.639Å) and π···π (3.511 and 3.774 Å) interactions. Introduction of TCM into the crystalline phases makes the molecular arrangement more compact with a number of strong intermolecular pairs such as C-H···π (2.541, 2.746, 2.789, 2.799, 2.898 and 3.105 Å), π···π (3.084 and 3.143 Å) and C=O···H-C (2.069 and 2.262 Å). From the theoretical calculation, such strengthened hydrogen bonding can lead to the red-shift of the C=O stretching vibration, from 1740.93 cm^{-1} in amorphous, 1736.21 cm^{-1} in crystal to 1711.36 cm^{-1} in cocrystal (Figure S6).

Nature of the low-lying excited states in aggregates

We then turned to look at the low-lying excited-states structure of Cz2BP, including excitation energies, natural transition orbitals (NTOs) contours and the SOC constants (ξ) for

the three aggregation states. The quantum mechanics/molecular mechanics (QM/MM) model is built as shown in Figure 2. Namely, we employ TDDFT/B3LYP/6-31G(d) to calculate the Cz2BP molecule embedded inside a cluster of molecules modeled by general amber force field in molecular mechanics.

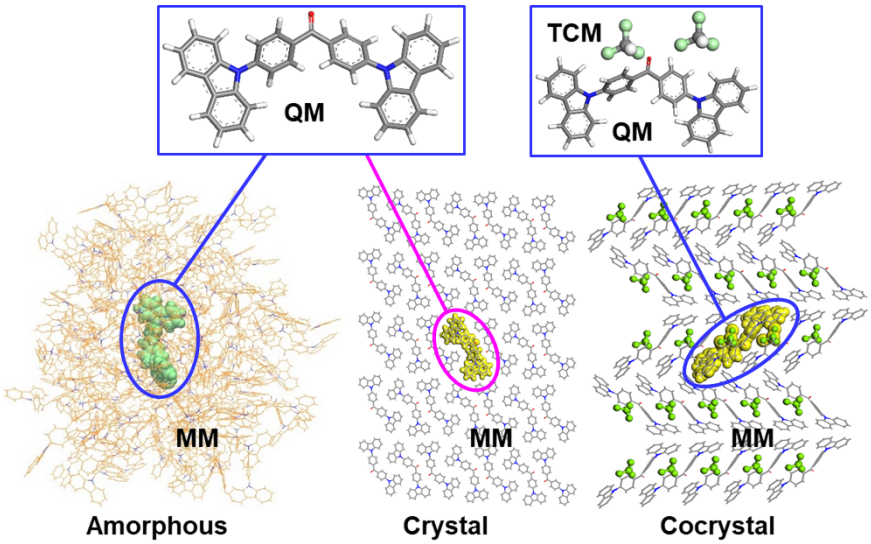

Figure 2. Setup of QM/MM models for Cz2BP in amorphous, crystal and cocrystal.

The calculated electronic structures are shown in Figures 3 and S7-S9, Table S1. We found that there are only two triplet states (T_1 and T_2) below the S_1 state for all the three cases. It is interesting that the electronic configurations of both S_1 and T_2 states are insensive to environments, which are dominated by the (π, π^*) transitions from π-orbital localized on cabazole groups to π^*-orbital concentrated on diphenylketone moiety as seen in Figures S8 and S9, Table S1. But for T_1 state, responsible for phosphorescence, the relative compositions of (n, π^*) and (π, π^*) strongly depends on the aggregation, namely, the (π, π^*) component in T_1 state is 59.8% in amorphous, 88.6% in crystal, and 94.6% in cocrystal, respectively. Such trend is in line with the results that the SOC coefficient ξ of $S_1 \rightarrow T_n$ (n=1, 2), which are all small (less than 0.33 cm^{-1}) in the three phases, while ξ for $T_1 \rightarrow S_0$ decreases from 17.22 cm^{-1}

in amorphous, 9.57 cm^{-1} in crystal to 5.52 cm^{-1} in cocrystal. In addition, the calculated vertical excitation energies of S_1 (2.62-2.81 eV) for amorphous structures (A0-A4) were well consistent with the experiment value (2.71 eV), see Table S2.

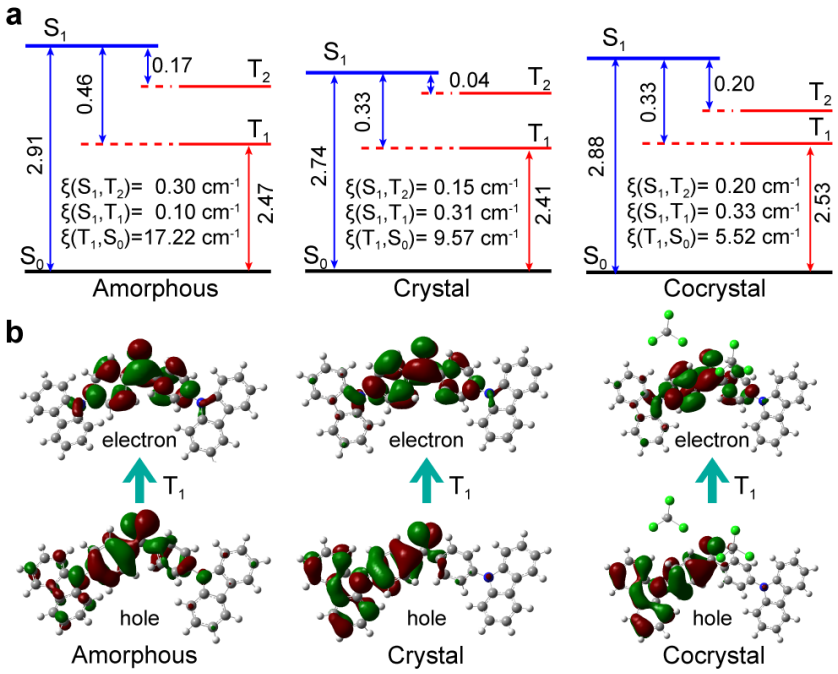

Figure 3. Calculated (a) energy diagram and SOC values of the low-lying excited states, and (b) natural transition orbitals (NTOs) of T_1 states for Cz2BP in amorphous, crystal and cocrystal forms. It is noted that the adiabatic excitation energy was employed.

Excited-state conversion and decay rates

To give a quantitative understanding on the aggregation-induced RTP, the excited-state conversion rates of $S_1 \rightarrow T_{1/2}$ and decay rates of $T_1/S_1 \rightarrow S_0$ were evaluated by using the thermal vibration correlation function (TVCF) formalism in our home-built MOMAP program,[37] and the results are depicted in Table 1. In TVCF, the radiative rate is evaluated by Einstein spontaneous emission relationship; and the non-radiative rate is based on Fermi-Golden Rule with both non-adiabatic coupling term and SOC term as the first-order perturbation in a

time-dependent formalism. For the three aggregation phases, the intersystem crossing rate constants (k_{isc}) of $S_1 \rightarrow T_2$ and $S_1 \rightarrow T_1$ all fell into the range of $\sim 10^6$-10^7 s^{-1}, being comparable to the corresponding radiative decay rate constants (k_f) of $S_1 \rightarrow S_0$ with $\sim 10^7 s^{-1}$, which indicates the triplet excitons can efficiently populated. Subsequently, it is found that the k_p of $T_1 \rightarrow S_0$ decreases about one order of magnitude from 4.78×10^1, 3.15×10^1 to 1.58 s^{-1} due to the decreasing oscillator strength f for T_1 (see Table S2). More importantly, the k_{nr} of $T_1 \rightarrow S_0$ is largely reduced by 3-6 orders of magnitudes from 1.87×10^6, 5.51×10^3 to 6.03 s^{-1}. It is noted that compared to the amorphous A0, the similar results for k_p and k_{nr} of $T_1 \rightarrow S_0$ are also obtained for Cz2BP amorphous A1-A4, see Table 1. Consequently, an efficient quantum yields ϕ_p (20.76%) of $T_1 \rightarrow S_0$ was given in cocrystal, in comparison to the extremely low ϕ_p in amorphous (<0.04%) and crystal (0.57%). Based on these results, it was concluded that the bright long-lived RTP of Cz2BP in cocrystal can be attributed to the big reducation in both k_p and k_{nr} for $T_1 \rightarrow S_0$. This mechanism is well different from previous ones of efficient ISC to harvest triplet exciton.[12,38-41] In addition, the calculated RTP lifetime $\tau_p = 208$ ms agrees well with experimental observation of value 353 ms, which proved the reliability of the current theoretical models.

Table 1. The calculated fluorescence radiative decay rate k_f, ISC rates k_{isc} of $S_1 \rightarrow T_n$ (n=1, 2), and radiative rate k_p, non-radiative decay rate k_{nr} and quantum efficiency $\phi_p = k_p/(k_p+k_{nr})$ of $T_1 \rightarrow S_0$, as well as the RTP lifetime $\tau_p = 1/(k_p+k_{nr})$ for Cz2BP in amorphous (A0-A4), crystal and cocrystal forms (T=300 K). The experimental lifetime was also listed as a comparison.

T=300 K	$S_1 \rightarrow S_0$	$S_1 \rightarrow T_2$	$S_1 \rightarrow T_1$	$T_1 \rightarrow S_0$					
	k_f (s^{-1})	k_{isc} (s^{-1})	k_{isc} (s^{-1})	k_p (s^{-1})	k_{nr} (s^{-1})	ϕ_p (%)		τ_p (ms)	
						Cal.	Exp.	Cal.	Exp.
A0	3.57×10^7	2.70×10^7	1.36×10^6	4.47×10^1	1.87×10^6	0.002	RTP ×	0.02	-
A1	1.56×10^7	-	-	3.06×10^1	6.67×10^4	0.046	RTP ×	0.46	-
A2	2.76×10^7	-	-	4.71×10^1	2.77×10^5	0.017	RTP ×	0.17	-
A3	5.12×10^7	-	-	4.97×10^1	1.16×10^6	0.004	RTP ×	0.04	-
A4	2.36×10^7	-	-	4.78×10^1	1.30×10^6	0.004	RTP ×	0.04	-
Crystal	4.43×10^7	4.14×10^6	2.21×10^7	3.15×10^1	5.51×10^3	0.57	RTP ×	5.68	-
Cocrystal	7.03×10^7	3.96×10^7	3.24×10^6	1.58	6.03	20.76	RTP √	208	353

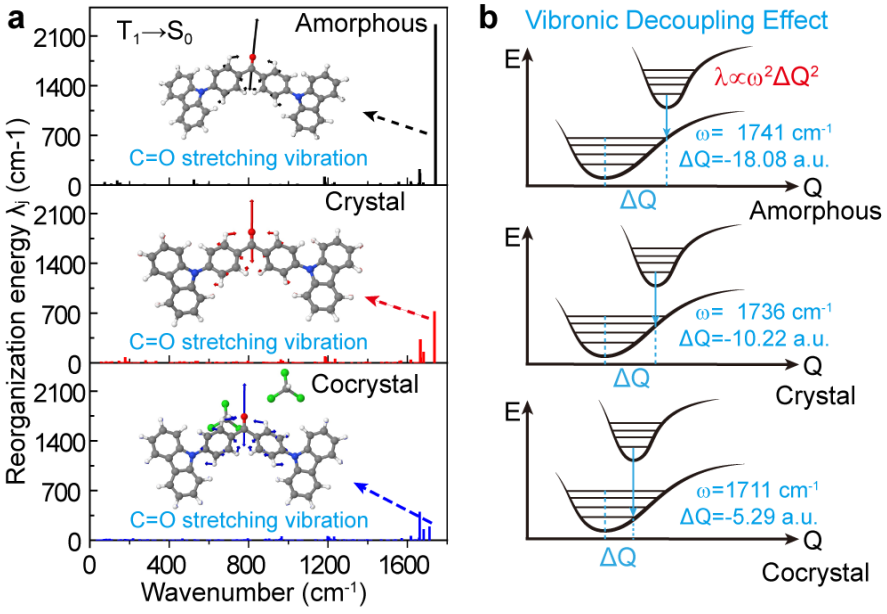

Figure 4. (a) Calculated normal mode reorganization energy λ_j of $T_1 \rightarrow S_0$ for amorphous, crystal and cocrystal forms of Cz2BP. (b) Illustration of the vibronic decoupling effect of electron and C=O stretching vibration from amorphous, crystal to cocrystal. It is noted that ω

is the vibration frequency and ΔQ is the normal modes displacement between two states (the values of C=O stretching vibration are listed).

The ISC rate is determined by the SOC matrix ξ and the density weighted Franck-Condon factor characterized by vibronic coupling or the reorganization energy λ.[42] Since the SOC values of $\xi(S_1,T_n)$ are small in all the aggregates, thus, small vibronic coupling must be responsible for the large ISC rate constant of $S_1 \rightarrow T_2$ and $S_1 \rightarrow T_1$. By analyzing λ in Figure S10, it is observed that (i) the normal modes in the low-frequency region (<400 cm^{-1}) contribute greatly, such as the out-of-plane vibration of benzene and carbazole units with the largest λ of ca. 200 cm^{-1} (inset in Figure S10); (ii) both the low-frequency and high-frequency modes contribute largely to the vibronic couplings for $S_1 \rightarrow T_1$ process (see Figure S10); (iii) and the vibronic couplings for $S_1 \rightarrow T_1$ and $S_1 \rightarrow T_2$ are all similar for the three aggregate phases, which lead to similar ISC rate constants. The major morphology dependence lies in the SOC constant for $T_1 \rightarrow S_0$ process $\xi(T_1,S_0)$, namely, from 17.22 cm^{-1} for amorphous, 9.57 cm^{-1} for crystal, to 5.52 cm^{-1} for cocrystal, see Figure 4, contributing one order of magnitude decreasing non-radiative decay rate k_{nr} according to $k_{nr} \propto \xi^2$. The remaining 3-5 orders of magnitude decrease in k_{nr} stem from the contributions from the vibronic couplings. The calculated λ given in Figures 4 and S11 indicate that the reorganization energies in low-frequency modes are all negligibly small and the primary contributions to total λ mainly come from the high-frequency modes (~1600-1700 cm^{-1}), including the stretching vibration of C=O bond and the breathing vibration of benzene and carbazole units. More strikingly, from amorphous, crystal to cocrystal, the reorganization energy of the C=O stretching vibration is drastically reduced from 1888.46, 717.24 to 186.67 cm^{-1}, with a shorten of

normal modes displacement ΔQ from -18.08, -10.22 to -5.29 a.u., mainly owing to the reduction of C=O bond length from 0.092, 0.064 to 0.043 Å between the S_0 and T_1 states (Table S3). Such a remarkable reduction is attributed to the decreased n-electrons density distribution at the oxygen atom seen from the hole NTO orbital. Solvent molecules TCM can move charge from carbonyl to benzene and carbazole units, as shown in Figure 3b, leading to a decoupling of electron to the C=O stretching vibration as the decrease of C=O bond length (see Figure 4b). It is due to such solvent induced vibronic decoupling leading to the eventual persistent RTP!

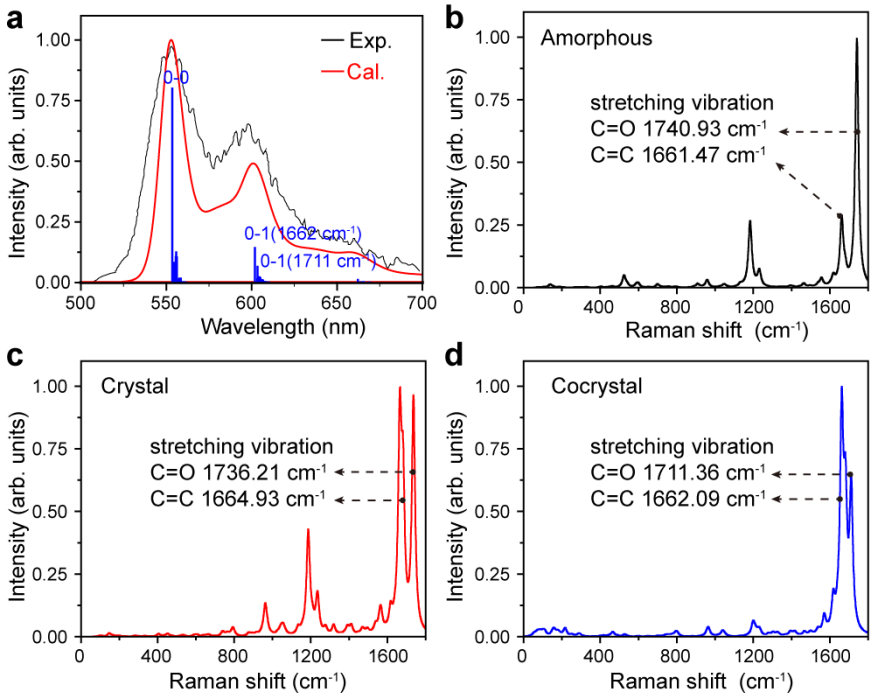

Figure 5. (a) The calculated phosphorescence spectra of Cz2BP in cocrystal with a red-shift of 0.14 eV to compare with the experimental ones at T=300 K. Predicted resonance Raman spectra for Cz2BP in (b) amorphous, (c) crystal and (d) cocrystal by using an incident wavelength of 480 nm, Lorentz broadening of 10 cm^{-1} and a damping factor of 100 cm^{-1}.

To independently verify the above proposed mechanism, we further calculate the

optical spectra. The calculated phosphorescence spectrum of Cz2BP in cocrystal phase is in comparison with the experiment, displayed in Figure 5a. It is worthwhile to note that: (i) the experimental spectra are fully reproduced by the theoretical results; (ii) the peak maximum around 550 nm corresponds to the 0-0 transition, indicating a weak vibronic coupling; (iii) the shoulder at ~ 600 nm is mainly attributed to the 0-1 transition for the C=C and C=O stretching with 1662 and 1711 cm^{-1}, respectively. Besides, we make theoretical predictions on the resonant Raman spectra for the three aggregate phases, as shown in Figure 5(b-d), waiting for the experimental verification. It is noted that the relative Raman intensity for C=O stretching with respect to C=C stretching mode is largely suppressed from amorphous, crystal to cocrystal. Such C=O stretching suppression is concomitant with increase of the $^3(\pi,\pi^*)$ proportion in T_1 states.

In summary, we present a computational study on the morphology dependent organic RTP for Cz2BP system from the perspective of hydrogen-bonding, excited states composition, and the vibronic couplings. MD simulations coupled with crystal prediction are performed to reproduce the amorphous conformations and the crystal structure. Subsequently, the QM/MM calculations were implemented to study the nature of low-lying excited states for Cz2BP in amorphous, crystal and cocrystal with TCM. Eventually, the excited-state conversion and decay rates and vibrationally resolved phosphorescence spectra are evaluated by the thermal vibration correlation function rate formalism in our home-built MOMAP program.

Going from amorphous, crystal to cocrystal, the intermolecular hydrogen bonding C=O···H-C distance is gradually decreased and makes a significant change in

electron-electron and electron-vibration interactions of the low-lying excited states, and determine the occurrence of the RTP. Impressively, (i) the T_1 state undergoes noticeable change from the mixed ($\pi/n\rightarrow\pi^*$) in amorphous and crystal phases to mainly ($\pi\rightarrow\pi^*$) transition with the latter composition increasing from 59.8%, 88.6% to 94.6%; (ii) the SOC coefficients for $S_1\rightarrow T_2$ and $S_1\rightarrow T_1$ fell into the region of 0.1-0.33 cm^{-1} for the three cases, but for $T_1\rightarrow S_0$ it decreases sharply from 17.22, 9.57 to 5.52 cm^{-1} due to the increase of ($\pi\rightarrow\pi^*$) transition component in T_1; (iii) the vibronic couplings are almost unchanged for $S_1\rightarrow T_2$ and $S_1\rightarrow T_1$ while for $T_1\rightarrow S_0$, it decreases drastically due to the hydrogen bond induced charge density decrease for the C=O bond; (iv) the ISC rate constants of $S_1\rightarrow T_2$ and $S_1\rightarrow T_1$ are in order of $\sim10^6$-10^7 s^{-1}, being comparable to the radiative rate constants of $S_1\rightarrow S_0$ with $\sim10^7$ s^{-1}. However, the k_{nr} of $T_1\rightarrow S_0$ is largely reduced by 3-6 orders of magnitude from 1.87×10^6, 5.51×10^3 to 6.03 s^{-1}, inducing a bright and long-lived RTP with a lifetime τ_p=208 ms (exp. 353 ms) for cocrystal. Namely, the vibronic decoupling of electron and C=O stretching vibration caused by the strong intermolecular hydrogen bond between Cz2BP and TCM is responsible for the long-lived RTP in cocrystal. The morphology dependent RTP is clearly explained by the intermolecular hydrogen bond effect on both the electronic configurations and electron-vibration couplings in the T_1 states. The presented results provide a new insight into RTP mechanism and a new design avenue to realize long-lived RTP by dopping some small common molecules for providing strong hydrogen bonds to phosphors.

ASSOCIATED CONTENT

Supporting Information. The computational details and results for crystal structure prediction and transition components, as well as reorganization energy of the low-lying excited states for Cz2BP in solid; the geometries and electronic structures of ground- and excited-states in amorphous, crystal and cocrystal.

AUTHOR INFORMATION

Corresponding Authors

*Qian Peng. Tel: +86-10-82616830. E-mail: qpeng@iccas.ac.cn.

*Zhigang Shuai. Tel: +86-10-62797689. E-mail: zgshuai@tsinghua.edu.cn.

Notes

The authors declare no competing financial interest.

ACKNOWLEDGMENTS

This work is supported by the National Natural Science Foundation of China (Grant Nos. 21788102, 21973043, 21973099, 91833302, 91622121, and 21875104), the Ministry of Science and Technology of China (Grant No. 2017YFA0204501), the Strategic Priority Research Program of the Chinese Academy of Sciences (Grant No. XDB12020200) and the Natural Science Foundation of the Jiangsu Higher Education Institutions (Grant No. 19KJB150010). We are grateful to the High Performance Computing Center in Nanjing Tech University and Tsinghua University for supporting the computational resources. The authors also thank Prof. Wenjian Liu for the providing BDF software for calculating SOCs.

REFERENCES

[1]. Nicol, A.; Kwok, R. T. K.; Chen, C.; Zhao, W.; Chen, M.; Qu, J.; Tang, B. Z. Ultrafast Delivery of Aggregation-Induced Emission Nanoparticles and Pure Organic Phosphorescent Nanocrystals by Saponin Encapsulation. *J. Am. Chem. Soc.* **2017,** *139*, 14792-14799.

[2]. Fateminia, S. M. A.; Mao, Z.; Xu, S.; Yang, Z.; Chi, Z.; Liu, B. Organic Nanocrystals with Bright Red Persistent Room-Temperature Phosphorescence for Biological Applications. *Angew. Chem. Int. Ed.* **2017,** *56*, 12160-12164.

[3]. Miao, Q.; Xie, C.; Zhen, X.; Lyu, Y.; Duan, H.; Liu, X.; Jokerst, J. V.; Pu, K. Molecular afterglow imaging with bright, biodegradable polymer nanoparticles. *Nat. Biotechnol.* **2017,** *35*, 1102-1110.

[4]. Goudappagouda; Manthanath, A.; Wakchaure, V. C.; Ranjeesh, K. C.; Das, T.; Vanka, K.; Nakanishi, T.; Babu, S. S. Paintable Room-Temperature Phosphorescent Liquid Formulations of Alkylated Bromonaphthalimide. *Angew. Chem. Int. Ed.* **2019,** *58*, 2284-2288.

[5]. He, Z.; Gao, H.; Zhang, S.; Zheng, S.; Wang, Y.; Zhao, Z.; Ding, D.; Yang, B.; Zhang, Y.; Yuan, W. Z. Achieving Persistent, Efficient, and Robust Room-Temperature Phosphorescence from Pure Organics for Versatile Applications. *Adv. Mater.* **2019,** *31*, 1807222.

[6]. Wang, X.-F.; Xiao, H.; Chen, P.-Z.; Yang, Q.-Z.; Chen, B.; Tung, C.-H.; Chen, Y.-Z.; Wu, L.-Z. Pure Organic Room Temperature Phosphorescence from Excited Dimers in Self-Assembled Nanoparticles under Visible and Near-Infrared Irradiation in Water. *J. Am. Chem. Soc.* **2019,** *141*, 5045-5050.

[7]. Kenry; Chen, C.; Liu, B. Enhancing the performance of pure organic room-temperature phosphorescent luminophores. *Nat. Commun.* **2019,** *10*, 2111.

[8]. Zhou, Y.; Qin, W.; Du, C.; Gao, H.; Zhu, F.; Liang, G. Long-Lived Room-Temperature Phosphorescence for Visual and Quantitative Detection of Oxygen. *Angew. Chem. Int. Ed.* **2019,** *58*, 12102-12106.

[9]. Li, C.; Tang, X.; Zhang, L.; Li, C.; Liu, Z.; Bo, Z.; Dong, Y. Q.; Tian, Y.-H.; Dong, Y.; Tang, B. Z. Reversible Luminescence Switching of an Organic Solid: Controllable On–Off

Persistent Room Temperature Phosphorescence and Stimulated Multiple Fluorescence Conversion. *Adv. Optical Mater.* **2015,** *3*, 1184-1190.

[10]. Yang, J.; Ren, Z.; Chen, B.; Fang, M.; Zhao, Z.; Tang, B. Z.; Peng, Q.; Li, Z. Three polymorphs of one luminogen: How the molecular packing affects the RTP and AIE properties? *J. Mater. Chem. C* **2017,** *5*, 9242-9246.

[11]. Xie, Y.; Ge, Y.; Peng, Q.; Li, C.; Li, Q.; Li, Z. How the Molecular Packing Affects the Room Temperature Phosphorescence in Pure Organic Compounds: Ingenious Molecular Design, Detailed Crystal Analysis, and Rational Theoretical Calculations. *Adv. Mater.* **2017,** *29*, 1606829.

[12]. Bian, L.; Shi, H.; Wang, X.; Ling, K.; Ma, H.; Li, M.; Cheng, Z.; Ma, C.; Cai, S.; Wu, Q.; et al. Simultaneously Enhancing Efficiency and Lifetime of Ultralong Organic Phosphorescence Materials by Molecular Self-Assembly. *J. Am. Chem. Soc.* **2018,** *140*, 10734-10739.

[13]. Zhang, T.; Zhao, Z.; Ma, H.; Zhang, Y.; Yuan, W. Z. Polymorphic Pure Organic Luminogens with Through-Space Conjugation and Persistent Room-Temperature Phosphorescence. *Chem. Asian J.* **2019,** *14*, 884-889.

[14]. Ma, H.; Lv, A.; Fu, L.; Wang, S.; An, Z.; Shi, H.; Huang, W. Room-Temperature Phosphorescence in Metal-Free Organic Materials. *Ann. Phys. (Berlin)* **2019,** *531*, 1800482.

[15]. Ma, X.; Wang, J.; Tian, H. Assembling-Induced Emission: An Efficient Approach for Amorphous Metal-Free Organic Emitting Materials with Room-Temperature Phosphorescence. *Acc. Chem. Res.* **2019,** *52*, 738-748.

[16]. Baroncini, M.; Bergamini, G.; Ceroni, P. Rigidification or interaction-induced phosphorescence of organic molecules. *Chem. Commun.* **2017,** *53*, 2081-2093.

[17]. Yuan, W. Z.; Shen, X. Y.; Zhao, H.; Lam, J. W. Y.; Tang, L.; Lu, P.; Wang, C.; Liu, Y.; Wang, Z.; Zheng, Q.; et al. Crystallization-Induced Phosphorescence of Pure Organic Luminogens at Room Temperature. *J. Phys. Chem. C* **2010,** *114*, 6090-6099.

[18]. Bolton, O.; Lee, K.; Kim, H.-J.; Lin, K. Y.; Kim, J. Activating efficient phosphorescence from purely organic materials by crystal design. *Nat. Chem.* **2011,** *3*, 205-210.

[19]. Gong, Y.; Zhao, L.; Peng, Q.; Fan, D.; Yuan, W. Z.; Zhang, Y.; Tang, B. Z.

Crystallization-induced dual emission from metal- and heavy atom-free aromatic acids and esters. *Chem. Sci.* **2015,** *6*, 4438-4444.

[20]. Gu, L.; Shi, H.; Bian, L.; Gu, M.; Ling, K.; Wang, X.; Ma, H.; Cai, S.; Ning, W.; Fu, L.; et al. Colour-tunable ultra-long organic phosphorescence of a single-component molecular crystal. *Nat. Photonics* **2019,** *13*, 406-411.

[21]. Wei, J.; Liang, B.; Duan, R.; Cheng, Z.; Li, C.; Zhou, T.; Yi, Y.; Wang, Y. Induction of Strong Long-Lived Room-Temperature Phosphorescence of N-Phenyl-2-naphthylamine Molecules by Confinement in a Crystalline Dibromobiphenyl Matrix. *Angew. Chem. Int. Ed.* **2016,** *55*, 15589-15593.

[22]. Yang, X.; Yan, D. Long-afterglow metal–organic frameworks: Reversible guest-induced phosphorescence tunability. *Chem. Sci.* **2016,** *7*, 4519-4526.

[23]. Cheng, Z.; Shi, H.; Ma, H.; Bian, L.; Wu, Q.; Gu, L.; Cai, S.; Wang, X.; Xiong, W.-w.; An, Z.; Huang, W. Ultralong Phosphorescence from Organic Ionic Crystals under Ambient Conditions. *Angew. Chem. Int. Ed.* **2018,** *57*, 678-682.

[24]. Wang, Z.; Zhu, C.-Y.; Yin, S.-Y.; Wei, Z.-W.; Zhang, J.-H.; Fan, Y.-N.; Jiang, J.-J.; Pan, M.; Su, C.-Y. A Metal–Organic Supramolecular Box as a Universal Reservoir of UV, WL, and NIR Light for Long-Persistent Luminescence. *Angew. Chem. Int. Ed.* **2019,** *58*, 3481-3485.

[25]. Wu, H.; Chi, W.; Chen, Z.; Liu, G.; Gu, L.; Bindra, A. K.; Yang, G.; Liu, X.; Zhao, Y. Achieving Amorphous Ultralong Room Temperature Phosphorescence by Coassembling Planar Small Organic Molecules with Polyvinyl Alcohol. *Adv. Funct. Mater.* **2019,** *29*, 1807243.

[26]. An, Z.; Zheng, C.; Tao, Y.; Chen, R.; Shi, H.; Chen, T.; Wang, Z.; Li, H.; Deng, R.; Liu, X.; Huang, W. Stabilizing triplet excited states for ultralong organic phosphorescence. *Nat. Mater.* **2015,** *14*, 685-690.

[27]. Lucenti, E.; Forni, A.; Botta, C.; Carlucci, L.; Giannini, C.; Marinotto, D.; Pavanello, A.; Previtali, A.; Righetto, S.; Cariati, E. Cyclic Triimidazole Derivatives: Intriguing Examples of Multiple Emissions and Ultralong Phosphorescence at Room Temperature. *Angew. Chem. Int. Ed.* **2017,** *56*, 16302-16307.

[28]. Yang, J.; Zhen, X.; Wang, B.; Gao, X.; Ren, Z.; Wang, J.; Xie, Y.; Li, J.; Peng, Q.; Pu,

K.; et al. The influence of the molecular packing on the room temperature phosphorescence of purely organic luminogens. *Nat. Commun.* **2018,** *9*, 840.

[29]. Yang, Z.; Mao, Z.; Zhang, X.; Ou, D.; Mu, Y.; Zhang, Y.; Zhao, C.; Liu, S.; Chi, Z.; Xu, J.; et al. Intermolecular Electronic Coupling of Organic Units for Efficient Persistent Room-Temperature Phosphorescence. *Angew. Chem. Int. Ed.* **2016,** *55*, 2181-2185.

[30]. Ma, H.; Shi, W.; Ren, J.; Li, W.; Peng, Q.; Shuai, Z. Electrostatic Interaction-Induced Room-Temperature Phosphorescence in Pure Organic Molecules from QM/MM Calculations. *J. Phys. Chem. Lett.* **2016,** *7*, 2893-2898.

[31]. Zhang, T. T.; Gao, H. Q.; Lv, A. Q.; Wang, Z. Y.; Gong, Y. Y.; Ding, D.; Ma, H. L.; Zhang, Y. M.; Yuan, W. Z. Hydrogen bonding boosted the persistent room temperature phosphorescence of pure organic compounds for multiple applications. *J. Mater. Chem. C* **2019,** *7*, 9095-9101.

[32]. Wang, Q.; Dou, X.; Chen, X.; Zhao, Z.; Wang, S.; Wang, Y.; Sui, K.; Tan, Y.; Gong, Y.; Zhang, Y.; et al. Reevaluating Protein Photoluminescence: Remarkable Visible Luminescence upon Concentration and Insight into the Emission Mechanism. *Angew. Chem. Int. Ed.* **2019,** *58*, 12667-12673.

[33]. Goswami, A.; Garai, M.; Biradha, K. Interplay of Halogen Bonding and Hydrogen Bonding in the Cocrystals and Salts of Dihalogens and Trihalides with N,N '-Bis(3-pyridylacrylamido) Derivatives: Phosphorescent Organic Salts. *Cryst. Growth Des.* **2019,** *19*, 2175-2188.

[34]. Taylor, R.; Wood, P. A. A Million Crystal Structures: The Whole Is Greater than the Sum of Its Parts. *Chem. Rev.* **2019,** *119*, 9427-9477.

[35]. Li, H.; Bahuleyan, B. K.; Johnson, R. P.; Shchipunov, Y. A.; Suh, H.; Ha, C.-S.; Kim, I. Morphology-tunable architectures constructed by supramolecular assemblies of α-diimine compound: Fabrication and application as multifunctional host systems. *J. Mater. Chem.* **2011,** *21*, 17938-17945.

[36]. Beran, G. J. O. Modeling Polymorphic Molecular Crystals with Electronic Structure Theory. *Chem. Rev.* **2016,** *116*, 5567-5613.

[37]. Niu, Y.; Li, W.; Peng, Q.; Geng, H.; Yi, Y.; Wang, L.; Nan, G.; Wang, D.; Shuai, Z. MOlecular MAterials Property Prediction Package (MOMAP) 1.0: a software package for

predicting the luminescent properties and mobility of organic functional materials. *Mol. Phys.* **2018,** *116*, 1078-1090.

[38]. Zhao, W.; He, Z.; Lam, J. W. Y.; Peng, Q.; Ma, H.; Shuai, Z.; Bai, G.; Hao, J.; Tang, B. Z. Rational Molecular Design for Achieving Persistent and Efficient Pure Organic Room-Temperature Phosphorescence. *Chem* **2016,** *1*, 592-602.

[39]. Chen, X.; Xu, C.; Wang, T.; Zhou, C.; Du, J.; Wang, Z.; Xu, H.; Xie, T.; Bi, G.; Jiang, J.; et al. Versatile Room-Temperature-Phosphorescent Materials Prepared from N-Substituted Naphthalimides: Emission Enhancement and Chemical Conjugation. *Angew. Chem. Int. Ed.* **2016,** *55*, 9872-9876.

[40]. Liu, H.; Gao, Y.; Cao, J.; Li, T.; Wen, Y.; Ge, Y.; Zhang, L.; Pan, G.; Zhou, T.; Yang, B. Efficient room-temperature phosphorescence based on a pure organic sulfur-containing heterocycle: folding-induced spin–orbit coupling enhancement. *Mater. Chem. Front.* **2018,** *2*, 1853-1858.

[41]. Shi, H.; Song, L.; Ma, H.; Sun, C.; Huang, K.; Lv, A.; Ye, W.; Wang, H.; Cai, S.; Yao, W.; et al. Highly Efficient Ultralong Organic Phosphorescence through Intramolecular-Space Heavy-Atom Effect. *J. Phys. Chem. Lett.* **2019,** *10*, 595-600.

[42]. Shuai, Z.; Peng, Q. Organic light-emitting diodes: theoretical understanding of highly efficient materials and development of computational methodology. *Natl. Sci. Rev.* **2017,** *4*, 224-239.

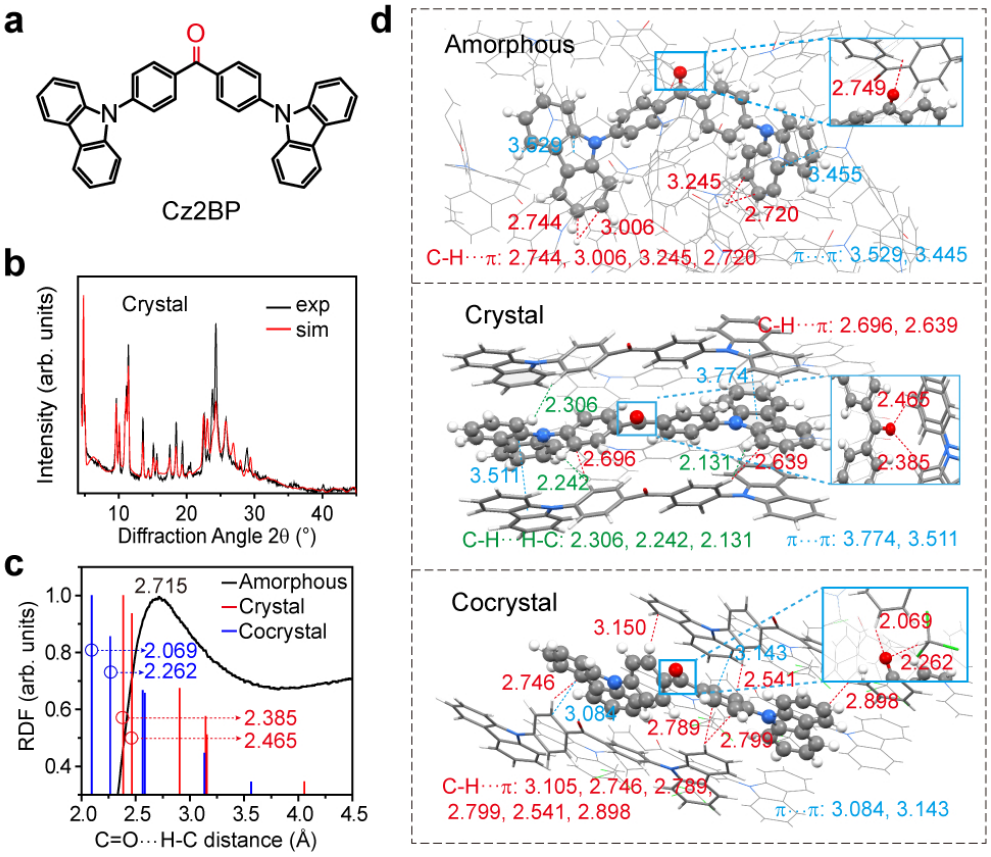

Figure 1. (a) Chemical structure of Cz2BP. (b) XRPD pattern of Cz2BP after refinement together with the experimental values and a difference plot. (c) The average radial distribution functions (RDFs) as a function of the intermolecular O-H distance for amorphous, crystal and cocrystal. (d) Perspective view of molecular packing in amorphous, crystal and cocrystal for Cz2BP. The unit is angstrom (Å).

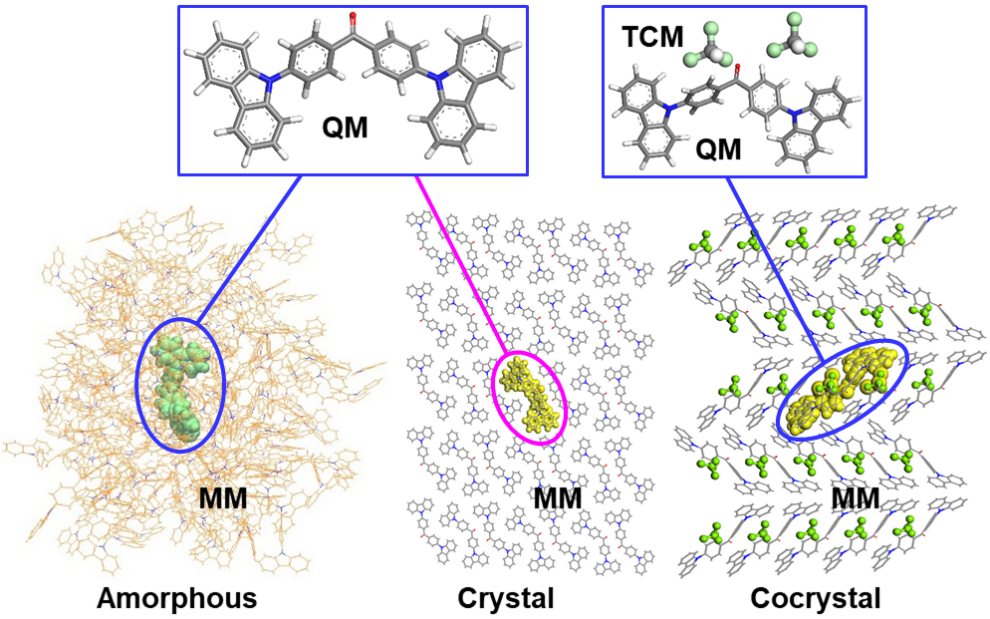

Figure 2. Setup of QM/MM models for Cz2BP in amorphous, crystal and cocrystal.

85x54mm (300 x 300 DPI)

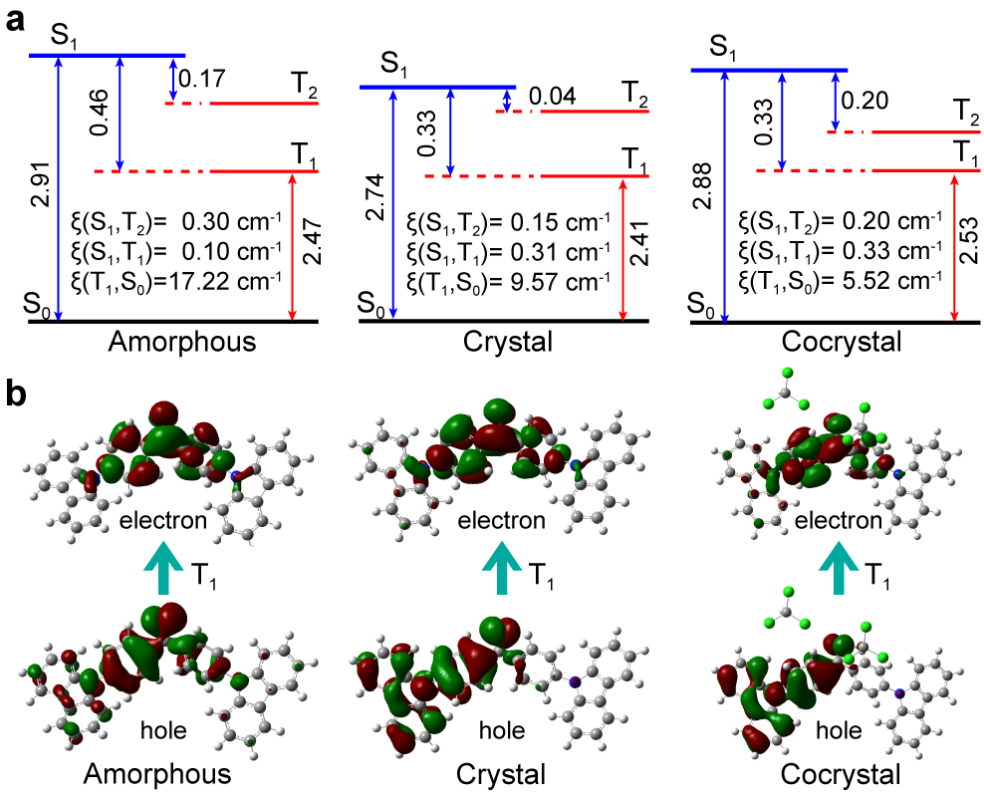

Figure 3. Calculated (a) energy diagram and SOC values of the low-lying excited states, and (b) natural transition orbitals (NTOs) of T1 states for Cz2BP in amorphous crystal and cocrystal forms. It is noted that the adiabatic excitation energy was employed.

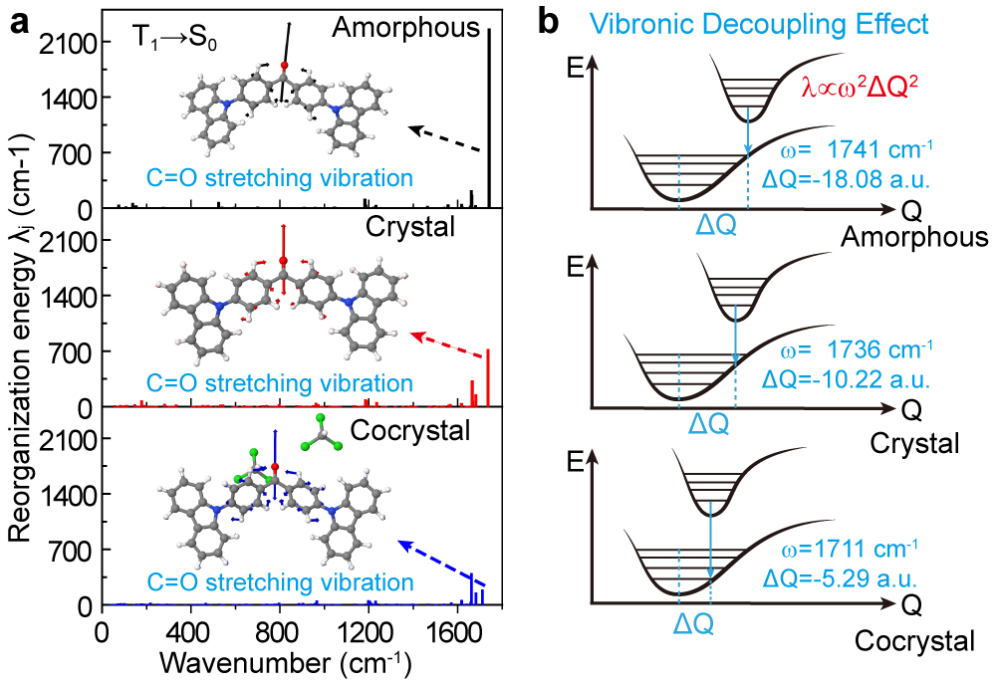

Figure 4. (a) Calculated normal mode reorganization energy λj of T1→S0 for amorphous, crystal and cocrystal forms of Cz2BP. (b) Illustration of the vibronic decoupling effect of electron and C=O stretching vibration from amorphous, crystal to cocrystal. It is noted that ω is the vibration frequency and ΔQ is the normal modes displacement between two states (the values of C=O stretching vibration are listed).

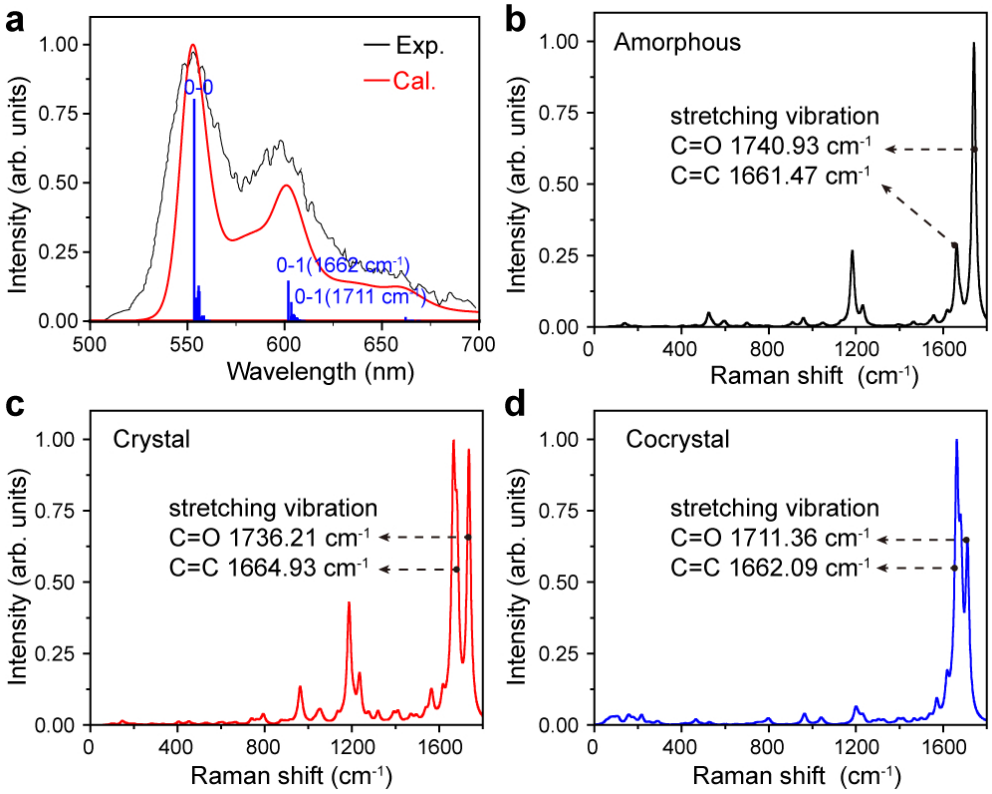

Figure 5. (a) The calculated phosphorescence spectra of Cz2BP in cocrystal with a red-shift of 0.14 eV to compare with the experimental ones at T=300 K. Predicted resonance Raman spectra for Cz2BP in (b) amorphous, (c) crystal and (d) cocrystal.

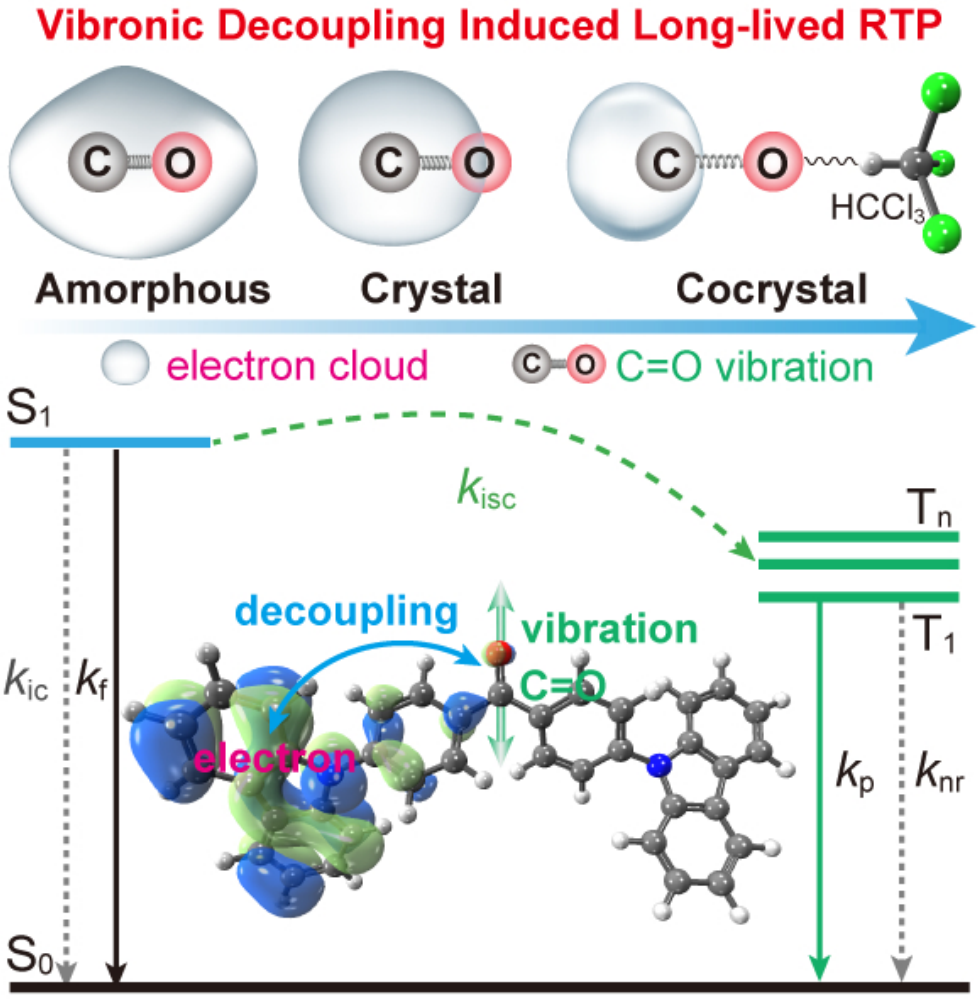
Vibronic Decoupling Induced Long-lived RTP
C
O
HCCl3
Amorphous
Crystal
Cocrystal
electron cloud
C=O vibration
S1
kisc
Tn
decoupling
vibration
C=O
T1
kic
kf
electron
kp
knr
S0

TOC